$$\%\,\text{Rutile} = \frac{1}{[(A/R)0.884 + 1]} \times 100$$

Where, A and R are the peak area for major anatase ($2\theta = 25^{\circ}$) and rutile phase ($2\theta = 28^{\circ}$), respectively.

Preparation of catalyst samples

A 20 wt% of Co/TiO_2 was prepared by the incipient wetness impregnation. A designed amount of cobalt nitrate [$Co(NO_3)\bullet 6H_2O$] was dissolved in deionized water and then impregnated onto TiO_2 containing various ratios of rutile:anatase obtained from above. The catalyst precursor was dried at 110°C for 12 h and calcined in air at 500°C for 4 h.

2.2 Catalyst nomenclature

The nomenclature used for the catalyst samples in this study is following:
Rn: titania support containing **n%** of rutile phase (R)
Co/Rn: titania support containing **n%** of rutile phase (R)-supported cobalt

2.3 Catalyst characterization

X-ray diffraction: XRD was performed to determine the bulk crystalline phases of catalyst. It was conducted using a SIEMENS D-5000 X-ray diffractometer with CuK_{α} (λ = 1.54439 Å). The spectra were scanned at a rate of 2.4 degree/min in the range 2θ = 20-80 degrees.

Scanning electron microscopy and energy dispersive X-ray spectroscopy: SEM and EDX were used to determine the catalyst morphologies and elemental distribution throughout the catalyst granules, respectively. The SEM of JEOL mode JSM-5800LV was applied. EDX was performed using Link Isis series 300 program.

Transmission electron microscopy (TEM): The dispersion of cobalt oxide species on the titania supports were determined using a JEOL-TEM 200CX transmission electron spectroscopy operated at 100 kV with 100k magnification.

Hydrogen chemisorption: Static H_2 chemisorption at 100°C on the reduced cobalt catalysts was used to determine the number of reduced surface cobalt metal atoms. This is related to the overall activity of the catalysts during CO hydrogenation. Gas volumetric chemisorption at 100°C was performed using the method described by Reuel and Bartholomew [6]. The experiment was performed in a Micromeritics ASAP 2010 using ASAP 2010C V3.00 software.

Temperature-programmed reduction: TPR was used to determine the reduction behaviors of the catalyst samples. It was carried out using 50 mg of a sample and a temperature ramp from 35 to 800°C at 5°C/min. The carrier gas was 5% H_2 in Ar. A cold trap was placed before the detector to remove water produced during the reaction.

3. RESULTS AND DISCUSSION

In this present study, we basically showed dependence of the number of reduced cobalt metal surface atoms on dispersion of cobalt oxides along with the presence of rutile phase in titania. Both XRD and SEM/EDX results (not shown) revealed good distribution of cobalt oxides over the titania support. However, it can not differentiate all samples containing various ratios of rutile/anatase phase. Thus, in order to determine the dispersion of cobalt oxide species on titania, a more powerful technique such as TEM was applied with all samples. The TEM micrographs for all samples are shown in Figure 1. The dark spots represented cobalt oxides species present after calcination of samples dispersing on titania consisting various

ratios of rutile:anatase. It can be observed that cobalt oxide species were highly dispersed on the titania supports for Co/R0, Co/R3, and Co/R19 samples resulting in an appearance of smaller cobalt oxide patches present. However, the degree of dispersion for cobalt oxide species essentially decreased with increasing the rutile phase in titania from 40 to 99% as seen for Co/R40, Co/R96, and Co/R99 samples resulting in the observation of larger cobalt oxide patches. It was suggested that the presence of rutile phase in titania from 0 (pure anatase phase) to 19% exhibited the highly dispersed forms of cobalt oxide species for the calcined samples. It is known that the active form of supported cobalt catalysts is cobalt metal (Co^0). Thus, reduction of cobalt oxide species is essentially performed in order to transform cobalt oxide species obtained after calcination process into the active cobalt metal atoms for catalyzing the reaction. Therefore, the static H_2 chemisorption on the reduced cobalt samples was used to determine the number of reduced Co metal surface atoms. This is usually related to the overall activity of the catalyst during carbon monoxide (CO) hydrogenation [7].

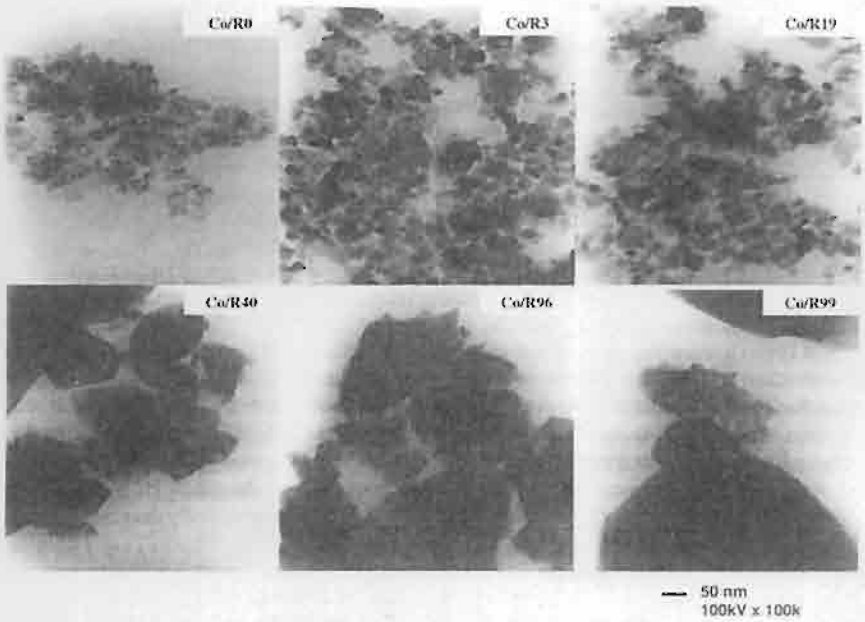

Figure 1 TEM micrographs of samples on various rutile/anatase ratios in titania

The resulted H_2 chemisorption for all samples revealed that the number of the reduced cobalt metal surface atoms increased with the presence of rutile phase in titania up to a maximum at 19% of rutile phase (Co/R19) before decreasing with the greater amounts of rultile phase as shown in **Table 1**. Considering the number of cobalt metal atoms for Co/R0 (pure anatase titania), the number was apparently low even though highly dispersed cobalt oxides species. This was suggested that highly dispersed forms of cobalt oxide species be not only the factor that insures larger number of reduced cobalt metal surface atoms in Co/TiO_2 [8]. On the other hand, it can be observed that the number of reduced cobalt metal surface atoms for Co/R40 and Co/R96 (with the low degree of dispersion of cobalt oxide species as seen by TEM) was

larger than that for Co/R0. This was due to the presence of rutile phase in Co/R40 and Co/R96. It should be mentioned that the largest number of reduced cobalt metal surface atoms for the Co/R19 sample was attributed to both highly dispersed cobalt oxide species and the presence of rutile phase in titania. In addition, the resulted TPR as also shown in Table 1 confirmed that the presence of rultie phase could facilitate the reduction of cobalt oxide species by lowering the reduction temperatures. As a result, the number of the reduced cobalt metal surface atoms increased.

Table 1 Resulted H_2 chemisorptiion and reduction temperatures for various Co/TiO_2 samples

Samples	Total H_2 Chemisorption (μmol H_2/g cat.)	Reduction Temperature ($^{\circ}$C)
Co/R0	0.93	370
Co/R3	1.55	270
Co/R19	2.44	320
Co/R40	1.66	285
Co/R96	1.71	275
Co/R99	0.69	275

4. SUMMARY

The present research showed a dependence of various ratios of rutile:anatase in titania as a catalyst support for Co/TiO_2 on characteristics, especially the reduction behaviors of this catalyst. The study revealed that the presence of 19% rutile phase in titania for Co/TiO_2 (Co/R19) exhibited the highest number of reduced Co metal surface atoms which is related the number of active sites present. It appeared that the increase in the number of active sites was due to two reasons; i) the presence of rutile phase in titania can facilitrate the reduction process of cobalt oxide species into reduced cobalt metal, and ii) the presence of rutile phase resulted in a larger number of reduced cobalt metal surface atoms. No phase transformation of the supports further occurred during calcination of catalyst samples. However, if the ratios of rutile:anatase were over 19%, the number of active sites dramatically decreased.

ACKNOWLEDGMENT

The financial support from the Thailand Research Fund (TRF) is greatly appreciated.

REFERENCES

[1] H.P. Wither, Jr., K.F. Eliezer, and J.W. Mechell, Ind. Eng. Chem. Res., 29 (1990)1807.
[2] J.L. Li, G. Jacobs, T. Das, and B.H. Davis, Appl. Catal. A., 233 (2002) 255.
[3] G. Jacobs, T. Das, Y.Q. Zhang, J.L. Li, G. Racoillet, and B.H. Davis., Appl. Catal. A., 233 (2002) 263.
[4] J.L. Li,, L.G. Xu, R. Keogh, and B.H. Davis, Catal. Lett., 70 (2000) 127.
[5] K.Y. Jung, and S.B. Park, J. Photochem. Photobio. A: Chem., 127 (1999) 117.
[6] R.C. Reuel, and C.H. Bartholomew, J. Catal., 85(1984) 63.
[7] B. Jongsomjit, C. Sakdamnuson, J.G. Goodwin, Jr., and P. Praserthdam, Catal. Lett., 94 (2004) 209.
[8] B. Jongsomjit, T. Wongsalee, and P. Praserthdam, Mater. Chem. Phys., 92 (2005) 572.

Available online at www.sciencedirect.com
ScienceDirect
Catalysis Communications 8 (2007) 548–556
CATALYSIS COMMUNICATIONS
www.elsevier.com/locate/catcom

Investigation of isosynthesis via CO hydrogenation over ZrO_2 and CeO_2 catalysts: Effects of crystallite size, phase composition and acid–base sites

Watcharapong Khaodee [a], Bunjerd Jongsomjit [a,*], Suttichai Assabumrungrat [a,*], Piyasan Praserthdam [a], Shigeo Goto [b]

[a] *Center of Excellence in Catalysis and Catalytic Reaction Engineering, Department of Chemical Engineering, Faculty of Engineering, Chulalongkorn University, Phyathai Road, Phatumwan, Bangkok 10330, Thailand*
[b] *Department of Chemical Engineering, Nagoya University, Chikusa, Nagoya 464-8603, Japan*

Received 29 March 2006; received in revised form 16 July 2006; accepted 2 August 2006
Available online 7 August 2006

Abstract

This paper investigates the isosynthesis via CO hydrogenation over zirconia and ceria catalysts. Various techniques including XRD, NH_3-TPD, CO_2-TPD and BET surface area were employed for the catalyst characterization. The results showed that not only acid–base properties, but also crystallite size and crystal phase essentially influenced the catalytic performance. It was found that the activity and the selectivity of isobutene in hydrocarbons on nanoscale catalysts were higher than those on the micronscale ones. Moreover, the acid–base properties were dependent on the fraction of tetragonal phase for zirconia, but independent on crystal phase for ceria. The synthesized nanoscale zirconias were more active than the commercial one but less than the nanoscale ceria. From the results, it was indicated that zirconia with 29% tetragonal phase exhibited the highest activity. Furthermore, the presence of tetragonal phase in zirconia played an important role on the selectivity of isobutene in hydrocarbons.

Keywords: CO hydrogenation; ZrO_2; CeO_2; Isobutene; Catalyst

1. Introduction

Isobutene, an extracted gas from C_4 stream of petroleum process, has been mainly used in the production of oxygenated compounds such as methyl *tert*-butyl ether (MTBE) and ethyl *tert*-butyl ether (ETBE). The trend of the octane enhancer demand is progressively increasing with the increased fuel consumption. Therefore the supply of isobutene from the petroleum product is possibly inadequate in the near future. It is expected that an alternative source for the production of isobutene needs to be explored. It is evident that one of the promising sources for isobutene synthesis can be achieved from a renewable resource such as biomass. It is known that fermentation of biomass produces methane and carbon dioxide. Both of these products can be used for synthesizing the syngas ($CO + H_2$), which can be subsequently converted to isobutene. Thus, advantages of this process are; (i) the chosen resource of isobutene production is renewable, then being more attractive than the conventional petroleum sources, which are about to shortage in the near future, (ii) carbon dioxide, a by-product of fermentation process, is substantially consumed to produce syngas, hence reducing the CO_2 emission to the atmosphere, and (iii) the ratio of carbon monoxide to hydrogen of 1:1 for the syngas from fermentation of biomass is suitable for the reaction of isobutene synthesis.

* Corresponding authors. Tel.: +662 218 6868; fax: +662 218 6877.
E-mail addresses: Bunjerd.J@chula.ac.th (B. Jongsomjit), Suttichai.A@chula.ac.th (S. Assabumrungrat).

1566-7367/$ - see front matter © 2006 Elsevier B.V. All rights reserved.
doi:10.1016/j.catcom.2006.08.001

It is recognized that the catalytic reaction that converts syngas to branched chain hydrocarbons, especially isobutane and isobutene, is so-called isosynthesis. As reported, the suitable catalysts for isosynthesis reaction are difficultly reducible oxides such as zirconia rather than other reduced transition metals [1]. It has been reported that zirconia was the most selective catalyst for isosynthesis [2–6]. Besides that, another oxide catalyst such as ceria (CeO_2) was also selective to isobutene in C_4 hydrocarbons [7]. Some researchers have tried to relate the characteristics of catalysts to their catalytic performance. For example, Su et al. [4] investigated the catalytic performance of various nanoscale zirconias for isosynthesis. They found that better formation of isobutene is resulted from higher ratio of base to acid sites on catalyst surface. In addition, effect of the crystal phase such as monoclinic phase in zirconia on the catalytic performance was also reported by Maruya et al. [6]. Because of the bifuntionality of zirconia, the acid–base properties could play an important role on the catalytic performance [4,8–10].

In this work, the catalytic performances of micron- and nanoscale zirconia and ceria on isosynthesis via CO hydrogenation were investigated. The synthesized nanoscale zirconia catalysts were prepared using the precipitation method with two different zirconium salt precursors. The synthesized nanoscale ceria was also prepared by the precipitation method. The catalytic performances and characteristics of the synthesized catalysts and commercial micron- and nanoscale zirconia and commercial micronscale ceria were also determined in order to eventually compare the effect of the crystallite size on the isosynthesis reaction.

2. Experimental

2.1. Catalyst preparation

The nanoscale zirconia (ZrO_2) was prepared by the precipitation method. It was carried out by slowly adding a solution of zirconium salt precursors such as zirconyl chloride ($ZrOCl_2$) or zirconyl nitrate [$ZrO(NO_3)_2$] (0.15 M) into a well-stirred precipitating solution of ammonium hydroxide (NH_4OH) (2.5 wt.%) at room temperature. The pH of the solution was carefully controlled at 10. The resulting precipitate was removed, and then washed with deionized water until Cl^- was not detected by a silver nitrate ($AgNO_3$) solution. The obtained sample was then dried overnight at 110 °C and calcined at 450 °C for 3 h with a temperature ramp of 1 °C/min. The synthesized zirconias obtained from $ZrOCl_2$ and $ZrO(NO_3)_2$ were denoted as ZrO_2–Cl (nano-syn) and ZrO_2–N (nano-syn), respectively. For a comparative study, another nanoscale zirconia was prepared by using zirconium *n*-propoxide 15 g as a starting material. The starting material was suspended in 100 ml of 1,5-pentanediol in the test tube, and then set up in 300 ml autoclave. In the gap between the test tube and autoclave wall, 30 ml of glycol was added. After the autoclave was completely purged with nitrogen, the autoclave was heated to 300 °C at the rate of 2.5 °C/min and held at that temperature for 2 h. Autogeneous pressure during the reaction gradually increased as the temperature was raised. After the reaction, the autoclave was cooled to room temperature. The resulting products were collected by repeatedly washed with methanol and centrifugation and then the products were dried in air. This synthesized zirconia was denoted as ZrO_2–PeG (nano-syn).

For the preparation of ceria (CeO_2), it was also prepared using the precipitation method as mentioned above. Cerium nitrate [$Ce(NO_3)_3$] was used as a cerium salt precursor. All conditions during preparation were the same as those for the zirconia preparation.

The commercial micron- and nanoscale zirconias named as the ZrO_2 (micron-com) and ZrO_2 (nano-com) and commercial micronscale ceria named as CeO_2 (micron-com) obtained from Aldrich were also used for the comparative study.

2.2. Catalyst characterization

2.2.1. N_2 physisorption

Measurements of BET surface area, cumulative pore volume and average pore diameter were performed by the N_2 physisorption using the Micromeritics ASAP 2020 surface area and porosity analyzer.

2.2.2. X-ray diffraction

The XRD spectra of catalysts were measured by a SIEMENS D5000 X-ray diffractometer using Cu Kα radiation with a nickel filter over the 2θ ranging from 20° to 80°. The crystal sizes of the prepared catalysts were obtained by XRD line broadening using Scherrer's equation. The characteristic peaks at $2\theta = 28.2°$ and 31.5° for (−1 1 1) and (1 1 1) reflexes, respectively, are assigned to the monoclinic phase in ZrO_2. The characteristic peak at $2\theta = 30.2°$ for the (1 1 1) reflex in the XRD patterns represents the tetragonal phase in ZrO_2. For the cubic fluorite phase in CeO_2, the XRD peaks at $2\theta = 28.6°$ and 33.1° are evident.

The percent of tetragonal and monoclinic phase in ZrO_2 was calculated by a comparison of the areas for the characteristic peaks of the monoclinic phase and the tetragonal phase. The percent of each phase was determined by means of the Gaussian areas $h \times w$, where h and w are the height and half-height width of the corresponding XRD characteristic peak as follows [4]:

$$\%\,\text{monoclinic phase} = \frac{\sum(h \times w)\text{monoclinic phase}}{\sum(h \times w)\text{monoclinic and tetragonal phase}},$$

$$\%\,\text{tetragonal phase} = \frac{\sum(h \times w)\text{tetragonal phase}}{\sum(h \times w)\text{monoclinic and tetragonal phase}}.$$

2.2.3. Transmission electron microscopy

Catalyst crystallite size and the diffraction pattern were obtained using the JEOL JEM-2010 transmission electron microscope operated at 200 kV with an optical point to point resolution of 0.23 nm at National Metal and Materials Technology Center (MTEC). The sample was dispersed in ethanol prior to the TEM measurement.

2.2.4. Temperature-programmed desorption

Temperature-programmed desorption of ammonia and carbon dioxide (NH_3- and CO_2-TPD) was used to determine the acid–base properties of catalysts. TPD experiments were carried out using a flow apparatus. The catalyst sample (0.1 g) was treated at its calcined temperature (450 °C) in helium flow for 1 h and then saturated with 15% NH_3/He mixture or pure CO_2 flow after cooling to 100 °C. After purging with helium at 100 °C for 1 h to remove weakly physisorbed NH_3 or CO_2, the sample was heated to 450 °C at a rate of 20 °C/min in a helium flow (50 cm^3/min). The amount of acid–base sites on the catalyst surface was calculated from the desorption amount of NH_3 and CO_2, respectively. It was determined by measuring the areas of the desorption profiles obtained from the Micromeritics ChemiSorb 2750 pulse chemisorption system analyzer.

2.3. Reaction procedure

CO hydrogenation was carried out at 400 °C and atmospheric pressure in a fixed-bed quartz reactor with a mixture of $CO/H_2/N_2 = 10/10/5$ cm^3/min. The catalyst sample of 2 g was used in each run. The reactor effluent samples were taken at 1.5 h interval and analyzed using the gas chromatography technique. Thermal conductivity detector (TCD) with molecular sieve 5A and Porapak-Q column was used to detect the CO and CO_2, respectively. The flame ionization detector (FID) with VZ-10 column was used to detect the light hydrocarbons such as C_1–C_4 hydrocarbons. The steady-state rate for all catalysts was obtained after 20 h.

3. Results and discussion

3.1. Physical properties

The XRD patterns of the commercial ZrO_2 and CeO_2 catalysts are shown in Fig. 1 and those of the synthesized ones are shown in Fig. 2. It showed that both commercial and synthesized CeO_2 catalysts exhibited the similar XRD peaks at $2\theta = 28.6°$ and 33.1° assigned to the typical cubic fluorite structure. However, based on the calculation, it showed that the average crystallite size for the commercial CeO_2 was in micronscale whereas the synthesized one was in nanoscale (Table 1). For the commercial micronscale ZrO_2 catalyst (Fig. 1), only the XRD peaks at $2\theta = 28.2°$ and 31.5° were observed indicating only the monoclinic phase in the micronscale ZrO_2. However, for the commercial nanoscale ZrO_2 catalyst (Fig. 1), besides the monoclinic characteristic peaks it also exhibited the XRD characteristic peaks of tetragonal at $2\theta = 30.2°$. For the synthesized ZrO_2 catalysts, ZrO_2–PeG (nano-syn) showed only tetragonal phase but ZrO_2–N (nano-syn) and ZrO_2–Cl (nano-syn) showed both of tetragonal and monoclinic phases. For all catalysts, the contents of different phases are listed in Table 1. Typically, the monoclinic phase is stable up to ca. 1170 °C and then, transforms into the tetragonal phase at higher temperature [11]. The tetragonal phase is stable up to ca. 2370 °C and finally transforms into the cubic phase at higher temperature. However, the metastable of the tetragonal phase in ZrO_2 can usually be observed when the precipitation method from an aqueous salt solution is employed as seen in this work or when the thermal decomposition of zirconium salts is used. Furthermore, the tetragonal phase appeared was attributed to size effect. Garvie [12] reported that the tetragonal phase appeared to be a critical crystallite size about 30 nm and above that point the tetragonal phase could not be stabilized at room

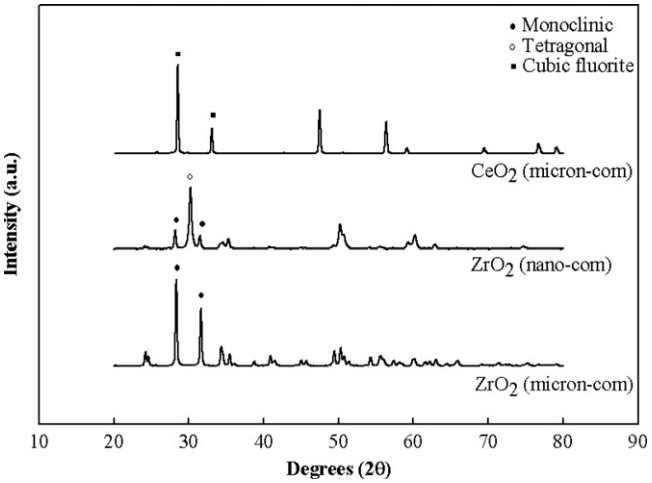

Fig. 1. XRD patterns of commercial ZrO_2 and CeO_2 catalysts.

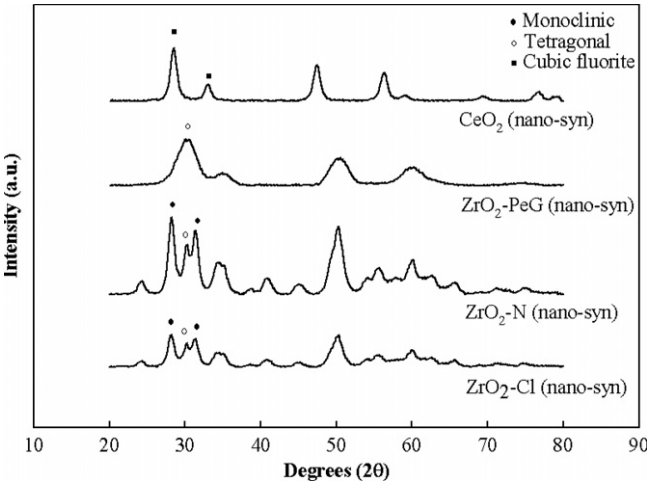

Fig. 2. XRD patterns of synthesized ZrO_2 and CeO_2 catalysts.

Table 1
Characteristics of ZrO_2 and CeO_2 catalysts

Catalysts	BET S.A.[a] (m^2/g)	Cumulative pore volume[b] (cm^3/g)	Average pore diameter[c] (nm)	Crystal size[d] (nm)			Crystal phase	Acid sites[h] (μmol/g)	Base sites[i] (μmol/g)
				M[e]	T[f]	C[g]			
ZrO_2 (micron-com)	6	0.012	9.5	65.8	–		100%M	24	15
ZrO_2 (nano-com)	41	0.115	9.9	30.3	22.2		30%M + 70%T	160	319
ZrO_2–Cl (nano-syn)	95	0.173	4.8	10.9	13.6		77%M + 23%T	361	191
ZrO_2–N (nano-syn)	92	0.169	4.9	9.8	8.3		71%M + 29%T	389	188
ZrO_2–PeG (nano-syn)	48	0.034	6.6	–	2.7	–	100%T	127	337
CeO_2 (micron-com)	4	0.008	16.6	–	–	135.9	100%C	16	9
CeO_2 (nano-syn)	91	0.149	4.7	–	–	8.1	100%C	190	161

[a] Error of measurement = ±5%.
[b] BJH desorption cumulative volume of pores between 1.7 and 300 nm diameter.
[c] BJH desorption average pore diameter.
[d] Determined by XRD line broadening using Scherrer's equation [17].
[e] Monoclinic phase in ZrO_2.
[f] Tetragonal phase in ZrO_2.
[g] Cubic phase in CeO_2.
[h] Measured by NH_3-TPD.
[i] Measured by CO_2-TPD.

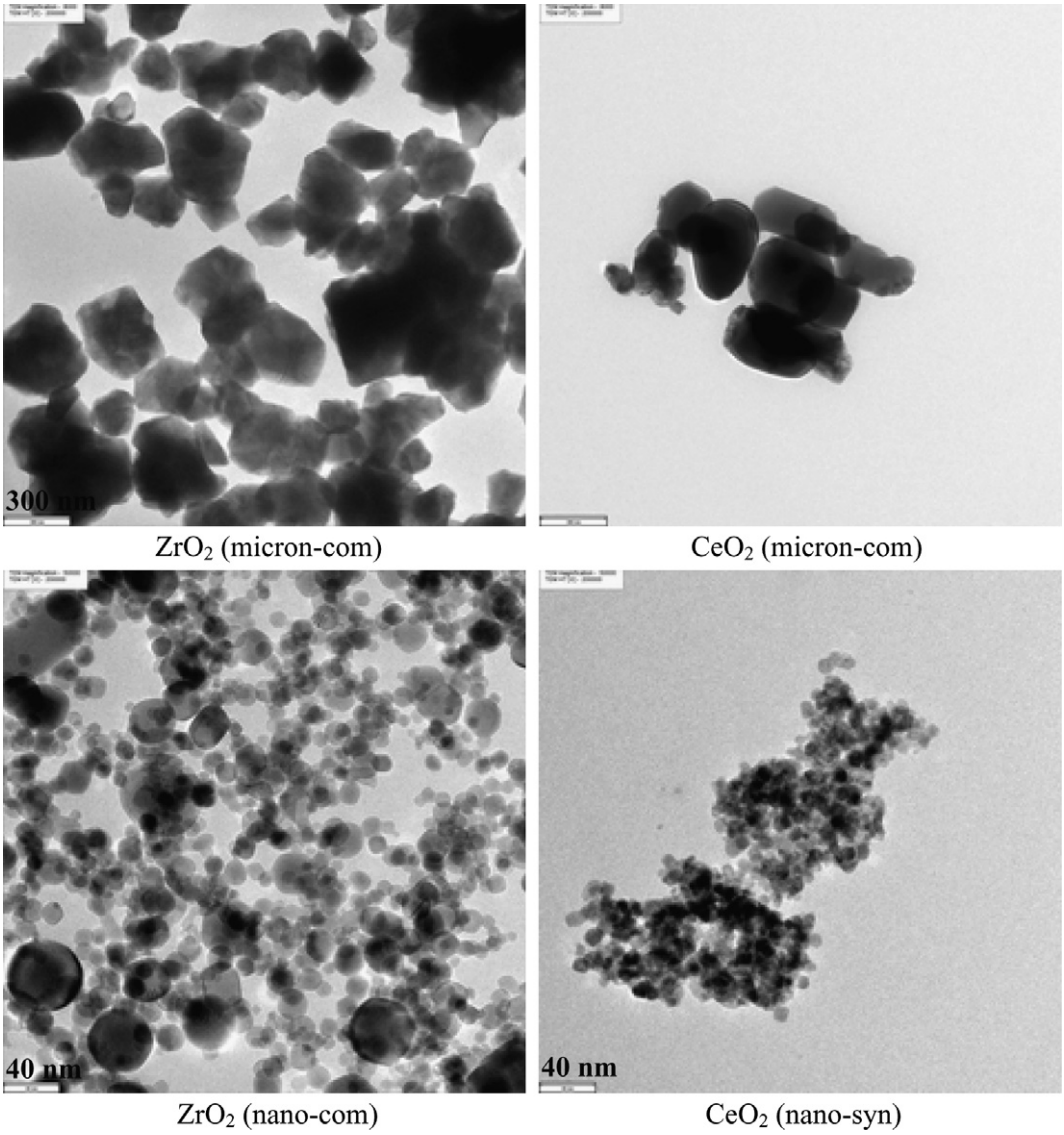

Fig. 3. TEM micrographs of ZrO_2 and CeO_2 catalysts.

temperature. The average crystallite sizes of each phase being present in all catalysts were calculated using the XRD line broadening regarding to its characteristic peaks. Thus, only the commercial micronscale ZrO_2 catalyst had no tetragonal phase because of its crystallite size was more than 30 nm. The crystallite sizes of catalysts can be determined by means of not only XRD technique, but also TEM technique. TEM provided the image of characteristics of particles indicating the crystallite size or the particle size. TEM micrographs of all catalysts are illustrated in Fig. 3. It was found that the commercial micronscale ZrO_2 and CeO_2 catalysts had the particle size more than 100 nm which absolutely indicated that these catalysts were in micron-sized. For the nanoscale catalysts, the average particle size indicated that these catalysts were in nano-sized and the values of them were similar to the values of crystallite sizes calculated by the XRD technique. Moreover, TEM with the electron diffraction mode can determine the crystallographic structure of catalyst. From the electron diffraction results (Fig. 4), it was revealed that both of the nanoscale ZrO_2 and CeO_2 catalysts were polycrystallite. The other physical properties of catalysts such as BET surface area, cumulative pore volume and average pore diameter are also summarized in Table 1. The micron- and nanoscale catalysts exhibited corresponding values based on their average crystallite sizes and BET surface areas. Compared to the micronscale catalysts, the nanoscale ones had smaller crystallite sizes which influenced not only on the increase in the cumulative pore volume, but also on the reduction of the average pore diameter. In contrast, the ZrO_2–PeG (nano-syn) had very small crystallite size, but low surface area. This was probably due to significantly less cumulative pore volume compared with other the nanoscale catalysts. For the ZrO_2 prepared by different zirconium salt precursors, the resulted crystal structure was probably changed [13]. Su et al. [5] and Wu

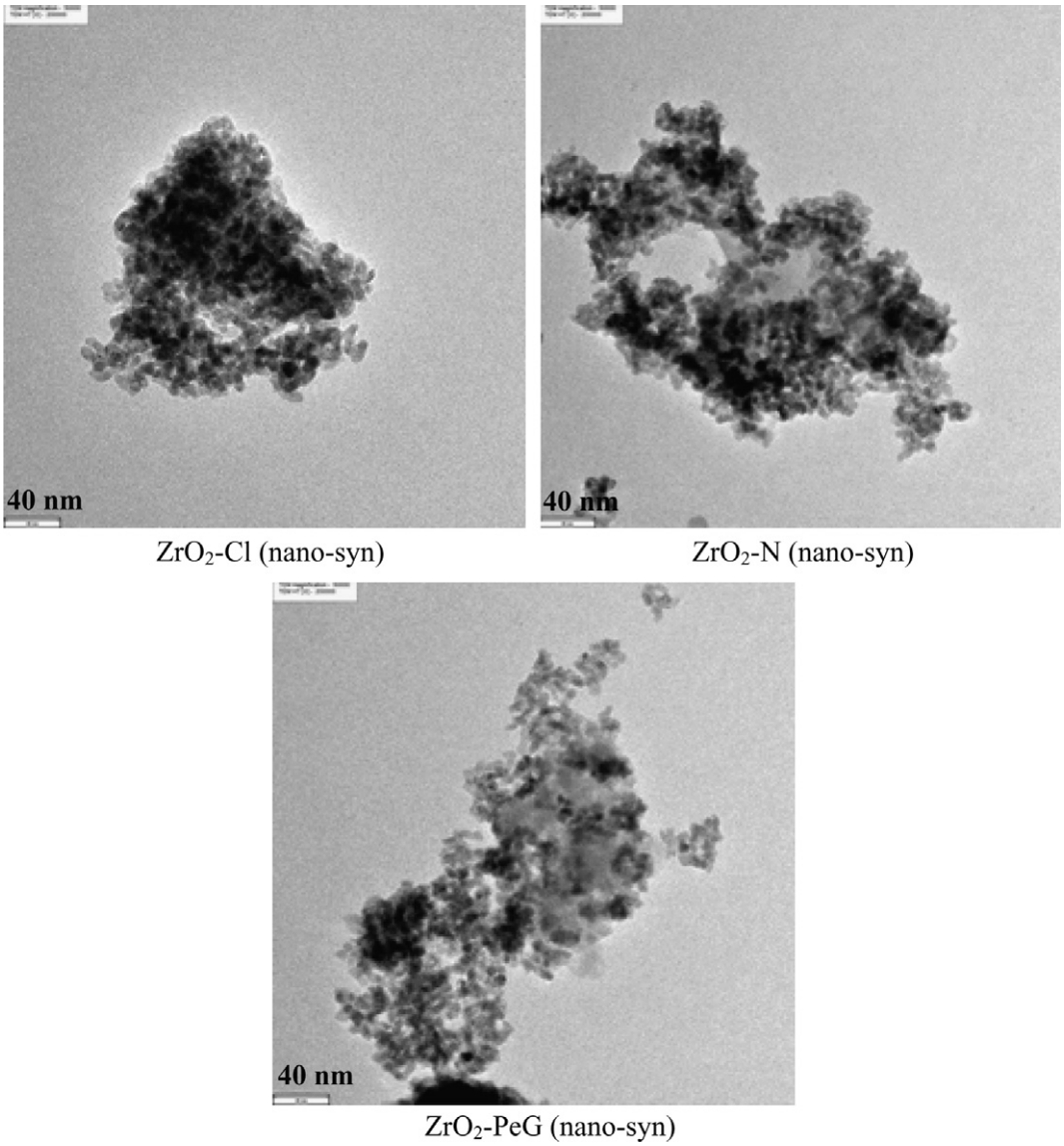

ZrO_2-Cl (nano-syn) ZrO_2-N (nano-syn)

ZrO_2-PeG (nano-syn)

Fig. 3 (*continued*)

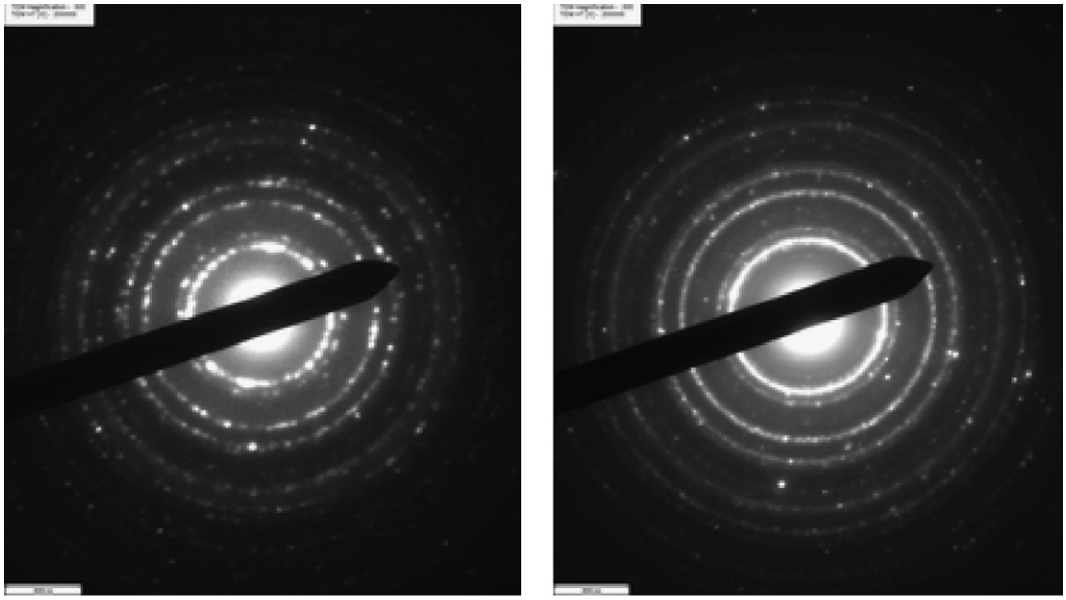

Fig. 4. TEM micrographs of nanoscale ZrO_2 and CeO_2 catalysts with electron diffraction mode.

and Yu [14] found that SO_4^{2-} from zirconium salt precursor such as $Zr(SO_4)_2$ affected crystallization and phase transformation of ZrO_2. The ZrO_2 prepared by $Zr(SO_4)_2$ showed both tetragonal phase and amorphous, but the ZrO_2 prepared by other zirconium salt precursors such as $Zr(NO_3)_4$, $ZrCl_4$ and $ZrOCl_2$ showed monoclinic and tetragonal phase. In this case, ZrO_2–Cl (nano-syn) and ZrO_2–N (nano-syn) were prepared using $ZrOCl_2$ and $ZrO(NO_3)_2$ as zirconium salt precursors, respectively. It was found that different precursors slightly affected the crystal structure in the phase composition of monoclinic/tetragonal phases over ZrO_2 and the BET surface area as well.

3.2. Acid–base properties

The acid–base properties of the catalysts were measured by NH_3- and CO_2-TPD, respectively. The NH_3- and CO_2-TPD profiles are shown in Figs. 5 and 6. From the TPD profiles, the amounts of acid and base sites which are also listed in Table 1 were calculated from the area below curve. The characteristic peaks of these profiles are assigned to their desorption temperatures indicating the strength of Lewis surface sites. From NH_3-TPD result of Ma et al. [15], it showed that NH_3 desorption peaks located at ca. 200 °C and 300 °C for ZrO_2 catalysts were corresponding to weak acid sites and moderate acid sites, respectively. Moreover, both peaks of monoclinic ZrO_2 exhibited slightly higher amount of acid sites compared to the tetragonal ZrO_2. In this work, all ZrO_2 mainly had weak acid sites whereas the moderate acid sites were evident for the ZrO_2–N (nano-syn). This was probably due to more fraction of monoclinic phase present. The other CeO_2 catalysts exhibited slightly different NH_3-TPD profiles of ZrO_2 catalysts.

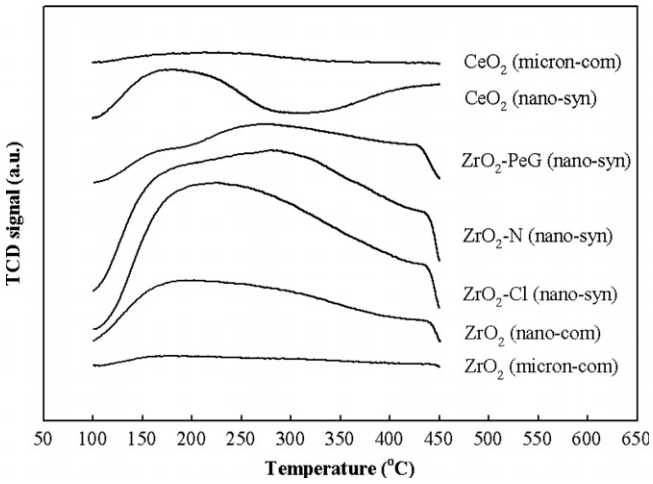

Fig. 5. NH_3-TPD profiles of catalysts.

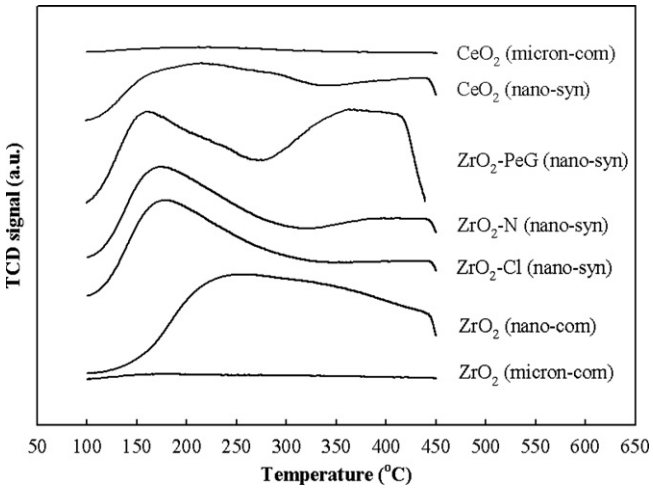

Fig. 6. CO_2-TPD profiles of catalysts.

Based on CO_2 desorption peaks, the weak base sites, moderate base sites and strong base sites can be identified [15]. It indicated that all kinds of base sites were presented in the tetragonal ZrO_2 whereas only weak and moderate base sites were observed on the monoclinic ZrO_2. For CO_2-TPD profiles of ZrO_2 (Fig. 6), the ZrO_2–PeG (nano-syn) exhibited higher desorption temperature than the other ZrO_2 catalysts due to pure tetragonal phase in ZrO_2. Furthermore, the ZrO_2–PeG (nano-syn) had the highest amount of base sites among the other ZrO_2 catalysts indicating higher basicity of tetragonal ZrO_2 than monoclinic ZrO_2. For the CeO_2 catalysts, it revealed only the weak base sites and moderate base sites. As a matter of fact, the ZrO_2 catalysts exhibited higher basicity than the CeO_2 catalysts. It should be mentioned that there were only a few acid and base sites for the micronscale catalysts (both ZrO_2 and CeO_2) compared to the nanoscale ones. It was suggested that differences in both acid and base sites can be attributed to the various fractions of crystal phases along with the crystallite sizes of catalysts. However, due to only one crystal phase in the ceria catalysts, the various acid and base sites present would be independent of crystal phase. Hence, different acid and base sites for ceria must be attributed to differences in crystallite sizes only. In fact, crystallite size also relates to BET surface area. Therefore, the amount of acid and base sites may be ascribed to effect of surface area. However, the two crystal phases of zirconia can be altered and consequently affected the acid–base properties. In order to give a better understanding, the relationship between acid–base sites and percent of tetragonal phase in ZrO_2 is illustrated in Fig. 7. It was found that the amount of acid sites increased with increased percents of tetragonal phase in ZrO_2 up to a maximum at ca. 29%, and then decreased with more tetragonal phase present. In other words, there was an optimum point at 29% of the tetragonal phase in ZrO_2, which can maximize the acid sites. Considering the base sites, the amount of base sites was apparently proportional to the percent of tetragonal phase in ZrO_2. As a result, basicity increased with increasing of tetragonal phase in ZrO_2.

3.3. Catalytic performance

The commercial ZrO_2 and CeO_2 catalysts and synthesized ones were tested for their isosynthesis activity and selectivity at 400 °C, atmospheric pressure and CO/H_2 of 1. A plot of reaction rates (based on products formed) versus the time-on-stream for all catalysts is shown in Fig. 8. Typically, time-on-stream behavior for CO hydrogenation exhibits the highest activity at initial time and gradually decreases with more reaction times until the reaction reaches the steady-state rate indicating a constant activity. Therefore, activity profiles for isosynthesis were similar to typical activity profiles CO hydrogenation. The steady-state rate was reached after 20 h and the value was shown in Table 2 along with the product selectivity. It was found that the catalytic activities of the commercial micronscale ZrO_2 and CeO_2 were low and the selectivities of isobutene in hydrocarbons were zero. No significant differences were observed regarding their physical properties. The acid–base sites for both micronscale catalysts were similar, but somehow, much lesser than those of the nanoscale ones. Therefore, the key factor that influenced the catalytic performance of the micronscale ZrO_2 and CeO_2 was essentially the amount of acid–base sites of these catalysts. From the previous works [4,8–10], it was reported that the catalytic activity and the selectivity of isobutene in hydrocarbons depended on the amount of acid and base sites of catalysts. The experimental results also revealed that the micronscale ZrO_2 was selective for C_3 in hydrocarbons, but the micronscale CeO_2 was selective for C_1 in hydrocarbons.

The synthesized nanoscale CeO_2 exhibited higher catalytic activity and selectivity of isobutene in hydrocarbons than the commercial micronscale one. It was found that the nanoscale CeO_2 had much higher BET surface area

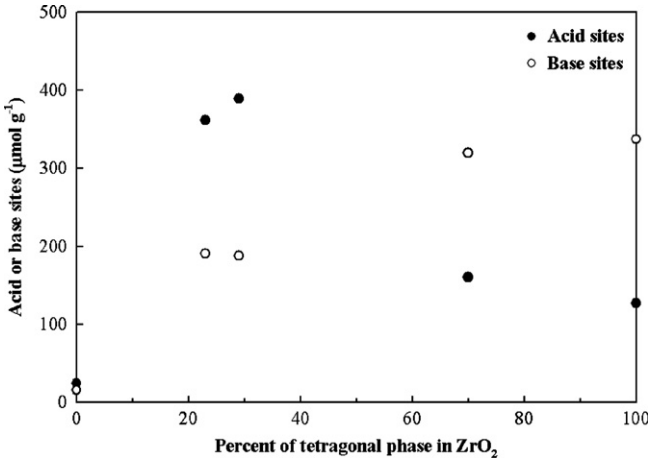

Fig. 7. Relationship between the amounts of acid–base sites and % tetragonal phase in ZrO_2.

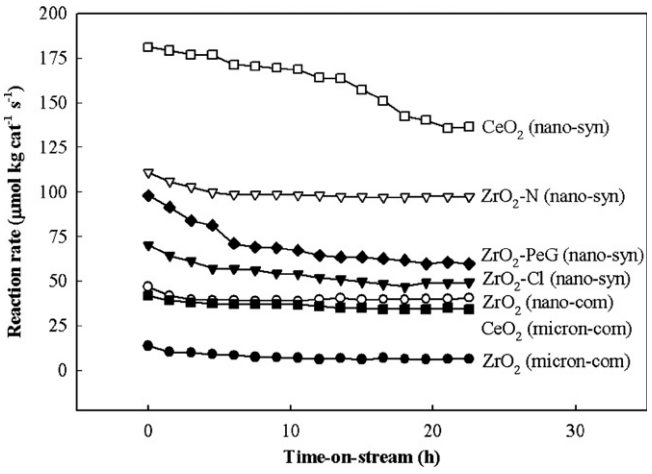

Fig. 8. Rate time profiles of catalysts on isosynthesis via CO hydrogenation.

Table 2
The catalytic performance of ZrO_2 and CeO_2 catalysts in the isosynthesis[a]

Catalysts	CO conversion (%)	Reaction rate[b] (μmol kg cat^{-1} s^{-1})	Product selectivity in hydrocarbons[c] (mol%)			
			C_1	C_2	C_3	i-C_4H_8
ZrO_2 (micron-com)	0.19	6.3	11.8	10.8 (88.4)	77.4 (100.0)	0.0
ZrO_2 (nano-com)	1.21	40.7	5.6	2.7 (59.0)	9.5 (91.6)	82.2
ZrO_2–Cl (nano-syn)	1.47	49.3	2.7	2.6 (72.6)	9.2 (96.3)	85.5
ZrO_2–N (nano-syn)	2.90	97.3	6.0	5.6 (60.4)	11.1 (87.9)	77.3
ZrO_2–PeG (nano-syn)	1.78	59.7	6.1	3.8 (67.0)	9.1 (95.9)	80.9
CeO_2 (micron-com)	1.02	34.3	69.2	8.8 (43.7)	22.0 (93.3)	0.0
CeO_2 (nano-syn)	4.07	136.4	9.4	14.4 (58.4)	18.6 (65.2)	57.6

[a] Reaction conditions were at 400 °C, 1 atm and $CO/H_2 = 1$.
[b] Steady state of reaction was reached at 20 h.
[c] Parentheses are percent of olefin being present in products.

and the amount of acid–base sites compared to the commercial micronscale one. Even though, the crystallite sizes of CeO_2 changed, the crystal phase of them was identical. Hence, it was suggested that the increase in BET surface area and/or the acid–base properties probably rendered the nanoscale CeO_2 catalyst high catalytic performance. The tendency of catalytic activity and selectivity of isobutene in hydrocarbons over the commercial micron- and nanoscale ZrO_2 was similar to those of CeO_2 according to the sizes. It was reported [2–6] that zirconia was the most selective catalyst in the isosynthesis and more effective than ceria [2,3], although it was also a selective catalyst for the formation of branched chain compounds such as isobutene in C_4 from syngas. Considering the commercial and synthesized nanoscale ZrO_2, the activity of the former exhibited less activity than the latter, but they had slightly difference in selectivity of isobutene in hydrocarbons (ca. 77–86%). The higher activity of the synthesized ZrO_2 could be due to higher amount of acid sites. The base property might slightly affect the reaction selectivity to isobutene, however, it was obscured by the higher activity. In this study, physical properties of the synthesized ZrO_2 with different zirconium salt precursor such as ZrO_2–Cl (nano-syn) and ZrO_2–N (nano-syn) did not change significantly. It was found that the ZrO_2–Cl (nano-syn) showed lower activity than the ZrO_2–N (nano-syn), which was possibly caused by lower amount of acid sites and a poison of Cl^-. The result of selectivity to isobutene decreased because of higher activity. Considering the catalytic performance reported by early researchers [5], the ZrO_2–Cl (nano-syn) showed higher activity, but lower selectivity of isobutene in hydrocarbons than the ZrO_2–N (nano-syn). This was probably due to different conditions of ZrO_2 preparation such as the precipitated pH.

It should be noted that the highest catalytic activity of ZrO_2 appeared at the highest amount of acid sites. Considering the base properties, the amount of base sites largely increased when the crystallite size was decreased from micron- to nano-sized, and then resulted in higher selectivity of isobutene in hydrocarbons. However, the nanoscale ZrO_2 at different amounts of base sites did not significantly change the selectivity of isobutene. Moreover, it was found that there was higher activity for the nanoscale CeO_2 compared to the nanoscale ZrO_2. This tendency was also similar to the case of the micronscale ZrO_2 and CeO_2 catalysts. The physical properties of both nanoscale catalysts were similar whereas the amount of acid and base sites of ZrO_2 was higher than those of CeO_2. However, the catalytic performance was changed to the opposite trend, which was perhaps due to the difference of crystal phase between ZrO_2 and CeO_2.

According to the relationship between acid–base properties and percent of tetragonal phase in ZrO_2 (Fig. 7), there was a maximum point at 29% tetragonal phase in ZrO_2 giving the highest amount of acid sites. It was the same trend as the relation of reaction rate and percent of tetragonal phase as shown in Fig. 9. It can be concluded that the catalytic activity apparently associated with acidity. Considering the relationship between selectivity of isobutene in hydrocarbons and tetragonal phase, it was proposed that the selectivities of isobutene were high and slightly changed when tetragonal phase appeared. In other words, the presence of tetragonal phase in zirconia rendered the better catalytic performance compared to with the absence of tetragonal phase.

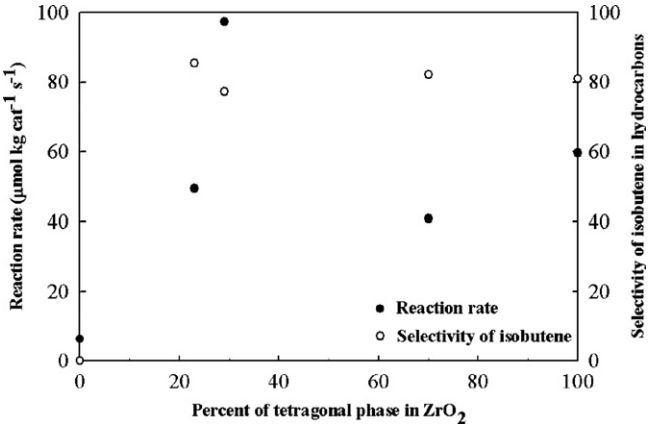

Fig. 9. Relationship between reaction rate, selectivity to isobutene in hydrocarbons and % tetragonal phase in ZrO_2.

In addition, it was reported that when compared the high reaction pressure to the low reaction pressure system, typically the latter exhibited lower catalytic activity, but higher selective of isobutene. Furthermore, lower reaction pressure may result in more selectivity of olefin, which was the same results as the previous work [6] than higher pressure system [4,5,8–10,16].

4. Conclusions

The comparison of catalytic performances in isosynthesis of various zirconia and ceria showed that nanoscale zirconia and ceria performed higher activity and selectivity of isobutene in hydrocarbons than micronscale ones. At the same crystallite size, ceria had higher activity than zirconia. The catalytic performances were dependent on crystallite sizes and amount of acid–base sites. It was indicated that the acid–base properties were dependent on the fraction of tetragonal phase for zirconia, but independent on crystal phase for ceria. The existence of tetragonal phase in zirconia rendered the high selectivity of isobutene in hydrocarbons.

Acknowledgements

The supports from the Thailand Research Fund and the Chulalongkorn University Graduate Scholarship commemoratory the 72nd Anniversary of H.M. Rama IX are greatly appreciated.

References

[1] I. Wender, Fuel Proc. Tech. 48 (1996) 189.
[2] H. Pichler, K.H. Ziesecke, Brennst. Chem. 30 (1949) 13.
[3] H. Pichler, K.H. Ziesecke, B. Traeger, Brennst. Chem. 30 (1949) 333.
[4] C. Su, J. Li, D. He, Z. Cheng, Q. Zhu, Appl. Catal. A: General 202 (2000) 81.
[5] C. Su, D. He, J. Li, Z. Chen, Q. Zhu, J. Mol. Catal. A: Chemical 153 (2000) 139.
[6] K. Maruya, T. Komiya, T. Hayakawa, L. Lu, M. Yashima, J. Mol. Catal. A: Chemical 159 (2000) 97.
[7] K. Maruya, K. Ito, K. Kushihashi, Y. Kishida, K. Domen, T. Onishi, Catal. Lett. 14 (1992) 123.
[8] Y. Li, D. He, Z. Cheng, C. Su, J. Li, Q. Zhu, J. Mol. Catal. A: Chemical 175 (2001) 267.
[9] Y. Li, D. He, Y. Yuan, Z. Cheng, Q. Zhu, Fuel 81 (2002) 1611.
[10] Y. Li, D. He, Q. Zhu, X. Zhang, B. Xu, J. Catal. 221 (2004) 584.
[11] P.D.L. Mercera, J.G. van Ommen, E.B.M. Doesburg, A.J. Burggraaf, J.R.H. Ross, Appl. Catal. 71 (1991) 363.
[12] R.C. Garvie, J. Phys. Chem. 82 (1978) 218.
[13] R. Srinivasan, B.H. Davis, Catal. Lett. 14 (1992) 165.
[14] F.C. Wu, S.C. Yu, J. Mater. Sci. 25 (1990) 970.
[15] Z.-Y. Ma, C. Yang, W. Wei, W.-H. Li, Y.-H. Sun, J. Mol Catal. A: Chemical 227 (2005) 119.
[16] Y. Li, D. He, Q. Zhang, B. Xu, Q. Zhu, Fuel Proc. Technol. 83 (2003) 39.
[17] H.P. Klug, L.E. Alexander, X-ray Diffraction Procedures for Polycrystalline Amorphous Materials, second ed., Wiley, New York, 1974.

Available online at www.sciencedirect.com
ScienceDirect
Applied Catalysis A: General 314 (2006) 128–133
APPLIED CATALYSIS A: GENERAL
www.elsevier.com/locate/apcata

Selective hydrogenation of acetylene in excess ethylene on micron-sized and nanocrystalline TiO_2 supported Pd catalysts

Joongjai Panpranot *, Kunyaluck Kontapakdee, Piyasan Praserthdam

Center of Excellence on Catalysis and Catalytic Reaction Engineering, Department of Chemical Engineering, Faculty of Engineering, Chulalongkorn University, Bangkok 10330, Thailand

Received 11 April 2006; received in revised form 22 July 2006; accepted 7 August 2006
Available online 20 September 2006

Abstract

Physicochemical properties and catalytic performances of Pd catalysts supported on commercial micron-sized and nanocrystalline TiO_2 synthesized by sol–gel and solvothermal method were studied for the selective hydrogenation of acetylene in the presence of excess ethylene. While acetylene conversions were found to be merely dependent on Pd dispersion, ethylene selectivity appeared to be strongly affected by the presence of Ti^{3+} in the TiO_2 samples. The use of pure anatase TiO_2 (either micron- or nano-sized) that contained significant amount of Ti^{3+} as supports for Pd catalysts gave high ethylene selectivities, while the use of pure rutile TiO_2 (without Ti^{3+} present) resulted in ethylene loss. The results suggest that the effect of Ti^{3+} on the TiO_2 supports was more important for high ethylene selectivity than the effect of TiO_2 crystallite size for selective acetylene hydrogenation over Pd/TiO_2 catalysts.

Keywords: Selective acetylene hydrogenation; Pd/TiO_2; Nanocrystalline TiO_2; Sol–gel; Solvothermal; Defect

1. Introduction

Removal of trace amount of acetylene in ethylene feed stream is vital for the commercial production of polyethylene since acetylene acts as a poison to the polymerization catalysts. In order to prevent ethylene loss, when acetylene is catalytically hydrogenated, it is desirable that ethylene remains intact during hydrogenation. Supported Pd-based catalyst is known to be the best catalyst so far for such reaction with good activity and selectivity. The commonly used support for palladium catalyst in selective acetylene hydrogenation is α-alumina, however, oligomer or green oil formation during reaction is inevitable over Pd/Al_2O_3 catalysts resulting in ethylene loss and shorten catalyst lifetime especially at high levels of acetylene conversion [1–6]. Several attempts to improve ethylene selectivity of the palladium catalyst have been made by many researchers, including incorporation of a second metal such as Ag [7–10], Au [11,12], Cu [13], Si [14], K [15], and Co [16], pre-treatment with oxygen-containing compounds such as CO and N_2O [17–20], and modification of the catalyst supports [21,22].

Among the various supports studied, TiO_2 is of particular interest because of its ability to manifest a strong metal–support interaction (SMSI) with group VIII metals and its low acidity compared to alumina. Moon and co-workers [21] reported an improved selectivity for ethylene production in selective acetylene hydrogenation over TiO_2-modified Pd catalysts. The authors suggest that charge transfer from Ti species to Pd weakened the adsorption strength of ethylene on the Pd surface hence higher ethylene selectivity was obtained. Moreover, the amount of green oil formation was reduced on the TiO_2-added Pd catalysts due to suppression of the multiply coordinated Pd sites resulting in an improved catalyst lifetime [23]. Fan and co-workers [24] studied selective hydrogenation of long chain alkadienes, it was shown that the presence of SMSI for Pd/TiO_2 catalysts led to higher selectivity of alkenes.

Recently, our group has reported the synthesis of nanocrystalline TiO_2 by solvothermal method and their applications as Pd catalyst supports in selective acetylene hydrogenation [25]. The solvothermal-derived TiO_2 supported Pd catalysts exhibited relatively high acetylene conversions and ethylene selectivities in the temperature range 40–90 °C in selective acetylene hydrogenation using trace amount of C_2H_2

* Corresponding author. Tel.: +66 2218 6878; fax: +66 2218 6877.
E-mail address: joongjai.p@eng.chula.ac.th (J. Panpranot).

0926-860X/$ – see front matter © 2006 Elsevier B.V. All rights reserved.
doi:10.1016/j.apcata.2006.08.024

in N_2 balance. Nevertheless, their catalytic activities and selectivities have not yet been compared to those of commercial TiO_2 supported ones under real commercial ethylene feed stocks. Thus, it is the aim of this study to investigate and compare the catalytic performances of commercial micron-sized and nanocrystalline TiO_2 supported Pd catalysts in selective acetylene hydrogenation in the presence of excess ethylene. The effects of crystallite size as well as other physicochemical properties such as the presence of Ti^{3+} defective sites of the TiO_2 on the catalytic properties of Pd/TiO_2 catalysts were investigated by means of X-ray diffraction (XRD), N_2 physisorption, X-ray photoelectron spectroscopy (XPS), CO chemisorption, scanning electron microscopy (SEM), and electron spin resonance (ESR).

2. Experimental

2.1. Preparation of TiO_2 and Pd/TiO_2 catalyst samples

The commercial anatase TiO_2 was obtained from Aldrich. By calcination in air at 1010 °C for 4 h using a space velocity of air flow 16,000 h^{-1}, the anatase TiO_2 was gradually transformed into rutile TiO_2. The commercial anatase and rutile TiO_2 were denoted as TiO_2-com-A and TiO_2-com-R, respectively.

Titanium ethoxide (Ti 20%) from Aldrich was used as Ti precursor for preparation of the nanocrystalline TiO_2 by sol–gel method [26]. A specific amount of the precursor was dissolved in ethanol and mixed with a water–ethanol solution at water to alkoxide molar ratio 165. The precursor solution was added drop wise to the aqueous solution and stirred by ultrasonic vibration at room temperature. White precipitates of hydrous oxides formed instantly and the mixture was stirred for at least two more hours. The amorphous precipitates were separated from the mother liquor by centrifugation and were re-dispersed in ethanol for five times to minimize particle agglomeration. The resulting materials were then dried and calcined at 450 °C in flowing oxygen for 2 h at the heating rate of 10 °C/min. The sol–gel derived TiO_2 was denoted hereafter as TiO_2-sol–gel.

The solvothermal-derived TiO_2 was prepared according to the method described in Ref. [27] using 25 g of titanium(IV) *n*-butoxide (TNB) 97% from Aldrich. The starting material was suspended in 100 ml of 1,4-butanediol in a test tube and then set up in an autoclave. In the gap between the test tube and autoclave wall, 30 ml of solvent was added. After the autoclave was completely purged with nitrogen, the autoclave was heated to 320 °C at 2.5 °C/min and held at that temperature for 6 h. Autogenous pressure during the reaction gradually increased as the temperature was raised. After the reaction, the autoclave was cooled to room temperature. The resulting powders were collected after repeated washing with methanol by centrifugation. They were then air-dried at room temperature. The solvothermal derived TiO_2 was denoted hereafter as TiO_2-solvothermal.

One percent Pd/TiO_2 were prepared by the incipient wetness impregnation technique using an aqueous solution of the desired amount of $Pd(NO_3)_2$ (Wako). The catalysts were dried overnight at 110 °C and then calcined in N_2 flow 60 cm^3/min with a heating rate of 10 °C/min until the temperature reached 500 °C and then in air flow 100 cm^3/min at 500 °C for 2 h.

2.2. Catalyst characterization

The BET surface areas of the samples were determined by N_2 physisorption using a Micromeritics ASAP 2000 automated system. Each sample was degassed under vacuum at <10 μm Hg in the Micromeritics ASAP 2000 at 150 °C for 4 h prior to N_2 physisorption. The XRD spectra of the catalyst samples were measured from 20–80° 2θ using a SIEMENS D5000 X-ray diffractometer and Cu Kα radiation with a Ni filter. Electron spin resonance spectra were taken at −150 °C using a JEOL JES-RE2X spectrometer. Relative percentages of palladium dispersion were determined by pulsing carbon monoxide over the reduced catalyst. Approximately 0.2 g of catalyst was placed in a quartz tube in a temperature-controlled oven. The amounts of CO chemisorbed on the catalysts were measured using a Micromeritic Chemisorb 2750 automated system attached with ChemiSoft TPx software at room temperature. Prior to chemisorption, the sample was reduced in a H_2 flow at 500 °C for 2 h then cooled down to ambient temperature in a He flow. The particle morphology was obtained using a JEOL JSM-35CF scanning electron microscope operated at 20 kV. Surface compositions of the catalysts were analyzed using an AMICUS photoelectron spectrometer equipped with a Mg Kα X-ray as a primary excitation and a KRATOS VISION2 software. XPS elemental spectra were acquired with 0.1 eV energy step at a pass energy of 75 kV. The C 1s line was taken as an internal standard at 285.0 eV.

2.3. Reaction study

Selective acetylene hydrogenation was performed in a quartz tube reactor (i.d. 9 mm). Prior to the start of each run, the catalyst was reduced in H_2 at 500 °C for 2 h. Then the reactor was purged with argon and cooled down to the reaction temperature, 40 °C. Feed gas composed of 1.46% C_2H_2, 1.71% H_2, 15.47% C_2H_6 and balanced C_2H_4 (Rayong Olefin Co., Ltd.) and a GHSV of 5400 h^{-1} were used. The composition of product and feed stream were analyzed by a Shimadzu GC 8A equipped with TCD and FID detectors (molecular sieve-5A and carbosieve S2 columns, respectively). Acetylene conversion as used herein is defined as moles of acetylene converted with respect to acetylene in feed. Ethylene selectivity is defined as the percentage of acetylene hydrogenated to ethylene over totally hydrogenated acetylene. The ethylene being hydrogenated to ethane (ethylene loss) is the difference between all the hydrogen consumed and all the acetylene which has been totally hydrogenated.

3. Results and discussion

3.1. Physicochemical properties of the TiO_2 supports

The SEM micrographs of various titania samples are shown in Fig. 1. The commercial anatase TiO_2 had a uniform particle

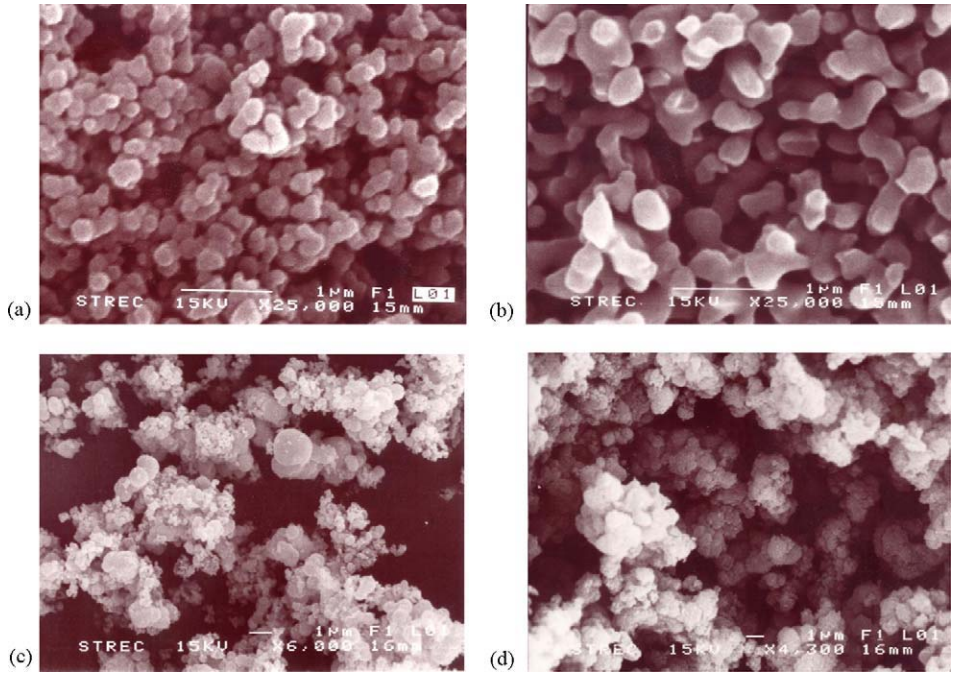

Fig. 1. SEM micrographs of: (a) TiO_2-com-A (b) TiO_2-com-R (c) TiO_2-sol–gel and (d) TiO_2-solvothermal.

size ca. 0.2 μm. After being subjected to thermal treatment (calcination) at 1010 °C for 4 h, pure anatase titania was gradually transformed into rutile titania and the particle size increased to ca. 0.4 μm. The morphology of pure anatase nanocrystalline TiO_2 prepared by sol–gel and solvothermal method was consisted of irregular shape of fine particles. However, some of the particles of those synthesized by the sol–gel method appeared to agglomerate into spherical micron-size particles. The crystallization mechanism of TiO_2 was probably different for these two methods resulting in different properties of the TiO_2 obtained. It was suggested that anatase titania synthesized by solvothermal in 1,4-butanediol was resulted from direct crystallization [27] while sol–gel method yielded a solid precipitate at relatively low temperature used and crystallization occurred during the subsequent calcination step. XRD patterns of the calcined TiO_2 samples are shown in Fig. 2. For the anatase titania (TiO_2-com-A, TiO_2-sol–gel, and TiO_2-solvothermal), XRD peaks at $2\theta = 25$ (major), 37, 48, 55, 56, 62, 71, and 75° 2θ were evident. The TiO_2-com-R exhibited XRD peaks for rutile phase at $2\theta = 28$ (major), 36, 42, and 57°. BET surface areas, average crystallite sizes, and percentages of atomic concentration (Ti/O) of the various TiO_2 samples are given in Table 1. The average crystallite sizes of the TiO_2 prepared by sol–gel and solvothermal calculated from the full width at half maximum of the XRD peak at $2\theta = 25°$ using Scherrer equation are in nanometer range (10 and 17, respectively) while those of the commercial ones could not be determined by this method due to the calculation limit of the Scherrer equation (the crystallite size may be too large). BET surface areas of the commercial anatase TiO_2 decreased essentially from 64.4 to 18.3 m^2/g after calcination in order to transform the crystalline phase to rutile phase TiO_2. It is surprising that the BET surface areas of the nano-sized TiO_2 prepared by sol–gel and solvothermal method were much lower

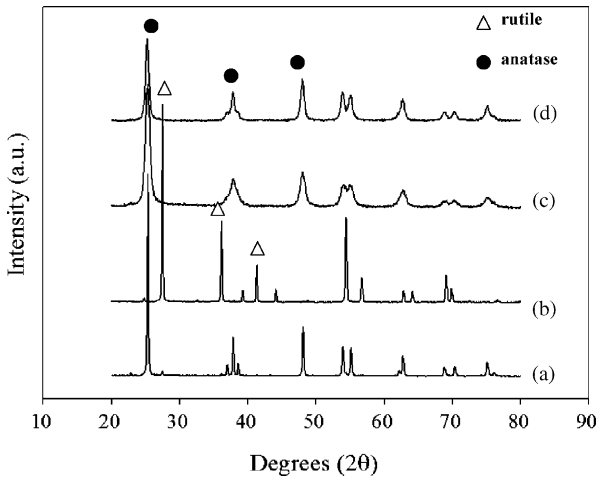

Fig. 2. XRD results of: (a) TiO_2-com-A (b) TiO_2-com-R (c) TiO_2-sol–gel and (d) TiO_2-solvothermal.

Table 1
Properties of the various TiO_2 supports

Sample	BET surface area[a] (m^2/g)	Crystallite size[b] (nm)	Atomic concentration[c] (%), Ti/O
TiO_2-com-A	64.4	n.d.	0.287
TiO_2-com-R	18.3	n.d.	0.250
TiO_2-sol–gel	39.3	10	0.232
TiO_2-solvothermal	26.8	17	0.220

[a] Error of measurement = ±10%.
[b] Determined from XRD line broadening.
[c] Determined from XPS analysis.

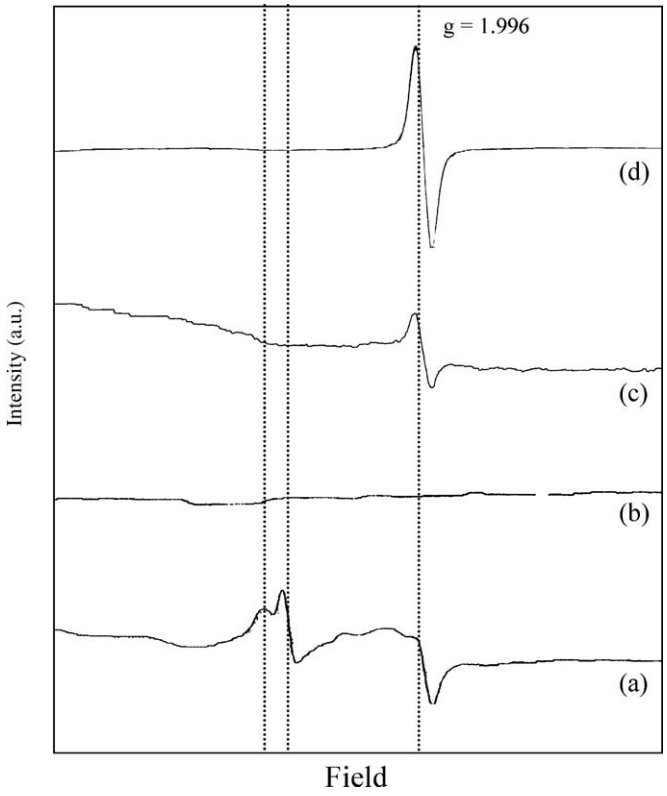

Fig. 3. ESR spectra of: (a) TiO_2-com-A (b) TiO_2-com-R (c) TiO_2-sol–gel and (d) TiO_2-solvothermal.

than that of the commercial anatase TiO_2. Such results suggest that the nano-crystals were closely packed resulting in low pore volume in the samples. Percentages of atomic concentrations of Ti and O on the surface of the TiO_2 were determined by the X-ray photoelectron spectroscopy. The Ti/O ratios were not significantly different among the four TiO_2 samples. There was probably an oxygen-rich layer near the surface of the TiO_2 particles, which is formed by oxygen adsorption and easy oxidation of titanium surface [28]. The ESR spectra of the TiO_2 samples are shown in Fig. 3. The signals of g values less than 2 were assigned to Ti^{3+} ($3d^1$) [29,30]. Nakaoka and Nosaka [31] reported six signals of ESR measurement occurring on the surface of titania: (i) $Ti^{4+}O^{-}Ti^{4+}OH^{-}$, (ii) surface Ti^{3+}, (iii) adsorbed oxygen (O^{2-}), (iv) $Ti^{4+}O^{2-}Ti^{4+}O^{2-}$, (v) inner Ti^{3+}, and

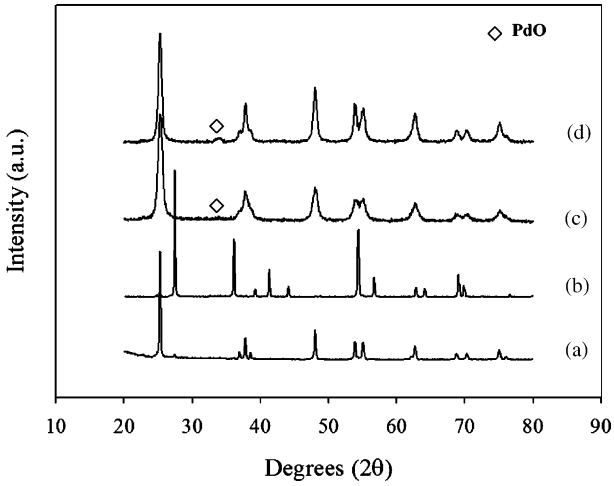

Fig. 4. XRD results of: (a) Pd/TiO_2-com-A (b) Pd/TiO_2-com-R (c) Pd/TiO_2-sol–gel and (d) Pd/TiO_2-solvothermal.

(vi) adsorbed water. In this study, it is seen that the sol–gel and solvothermal-derived TiO_2 exhibited only one signal at g value of 1.996 which can be attributed to Ti^{3+} at the surface. Many Ti^{3+} ESR signals were observed for the commercial anatase TiO_2, it is indicated that more than one type of Ti^{3+} defects were presented in the sample, i.e. surface Ti^{3+} and inner Ti^{3+}. It should be noted that the Ti^{3+} ESR signal was observed only for the anatase TiO_2 (both micron- and nano-sized). The rutile TiO_2 did not exhibit any ESR signal. It is suggested that Ti^{4+} in the rutile TiO_2 is more difficult to be reduced to Ti^{3+}. As rutile titania is more thermodynamically and structurally stable than anatase titania so that the Ti^{3+} ions fixed in the surface lattice of anatase TiO_2 is easier to diffuse to the surface than one in the surface lattice of rutile TiO_2 [24]. The intensity of the Ti^{3+} signal was highest for the solvothermal-derived TiO_2 suggesting that this preparation method produces the highest amount of defects on the TiO_2.

3.2. Characteristics and catalytic properties of Pd/TiO_2 catalysts

The XRD patterns of the various Pd/TiO_2 catalysts are shown in Fig. 4. There were no changes in the crystalline phase of the TiO_2 after impregnation of palladium for all the catalyst samples. The major XRD characteristic peak for PdO at $2\theta = 33.8^\circ$ were

Table 2
Characteristics of the various TiO_2-supported Pd catalysts

Catalyst	BET surface area[a] (m^2/g)	CO pulse chemisorption[b] ($\times 10^{-18}$ molecule CO/g catalyst)	Pd dispersion[c] (%)	d_P[d] Pd^0 (nm)	Atomic concentration[e] (%)	
					Ti/O	Pd/Ti
Pd/TiO_2-com-A	44.5	2.23	3.93	28.5	0.253	0.084
Pd/TiO_2-com-R	17.2	1.55	2.73	41.0	0.240	0.168
TiO_2-sol–gel	33.8	1.19	2.10	53.3	0.282	0.011
Pd/TiO_2-solvothermal	26.0	0.49	0.86	130.2	0.274	0.006

[a] Error of measurement = ±10%.
[b] Error of measurement = ±5%.
[c] Based on the total amount of palladium loaded.
[d] Based on $d = 1.12/D$ (nm), where D = fractional metal dispersion [34].
[e] Determined from XPS analysis.

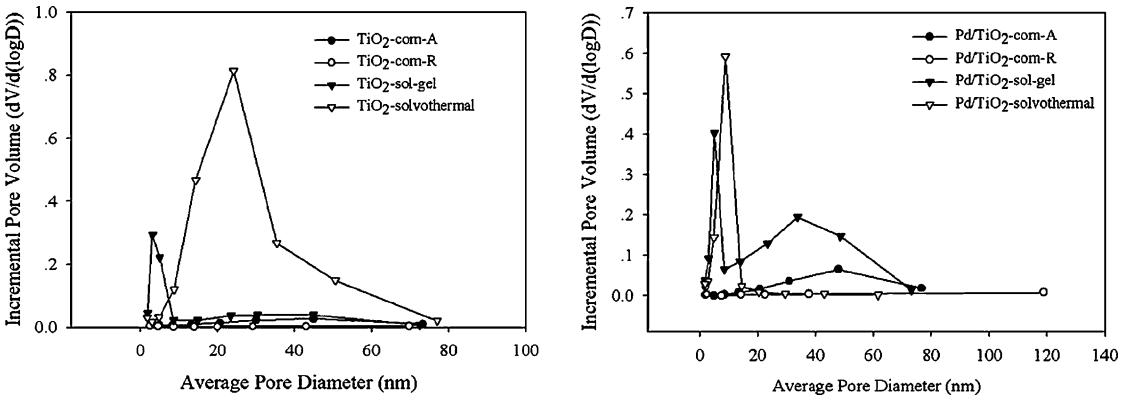

Fig. 5. Pore size distribution results of the various Pd/TiO_2 catalysts.

evident only for the catalyst prepared with the solvothermal-derived TiO_2. The BET surface areas, CO chemisorption results, and atomic concentration of surface element of the Pd/TiO_2 catalyst samples are given in Table 2. The BET surface area of the Pd catalysts were not significantly different form the original TiO_2 supports, however, changes in the pore size distribution of the catalysts due to Pd loading were observed for both sol–gel and solvothermal-derived TiO_2 supported ones suggesting that Pd was deposited in some of the pores of the TiO_2 (Fig. 5). It should also be noted that Pd/TiO_2-com-A was not heat-treated prior to the impregnation step, while the other supports were treated at 1010, 450, and 320 °C. Accordingly, it is also possible that a large decrease in the surface area of the anatase supported catalyst is caused by the calcination of the catalyst at 500 °C after the Pd loading. The percentages of Pd dispersion calculated from the CO chemisorption results were in the order Pd/TiO_2-com-A > Pd/TiO_2-com-R > Pd/TiO_2-sol–gel > Pd/TiO_2-solvothermal. The largest Pd particle size calculated from the CO chemisorption for the Pd/TiO_2-solvothermal catalyst is in a good agreement with the XRD results. It should be noted that as the anatase TiO_2 was transformed to rutile phase TiO_2, the amount of CO chemisorption decreased from 2.23×10^{18} to 1.55×10^{18} molecules CO while the calculated average particle size of Pd^0 metal increased from 28.5 to 41.0 nm. Thus, the presence of rutile phase significantly decreased dispersion of palladium on the titania supports. XPS analysis revealed an increasing Pd/Ti surface concentration from 0.084 to 0.168 when rutile TiO_2 was employed instead of anatase TiO_2. In contrast, the Pd/Ti atomic concentration ratios for those supported on sol–gel and solvothermal derived TiO_2 were much lower than those of the commercial TiO_2 supported ones.

In order to investigate the catalytic performance of the different types of TiO_2 supported Pd catalysts, selective hydrogenation of acetylene in excess ethylene was performed in a fixed bed flow reactor. Fig. 6 shows acetylene conversions and ethylene selectivities obtained from the various Pd/TiO_2 catalysts. Acetylene conversions were in the range of 20–59% and were found to be merely dependent on the Pd dispersion. The selectivities of ethylene were varied from −1.4 to 76.2% with the commercial rutile and the sol–gel derived TiO_2 supported Pd catalysts exhibited the lowest and the highest selectivities, respectively. However, it should be noted that the high ethylene selectivities of the nano-TiO_2 supported Pd catalysts may be because their conversions of acetylene were low. It is thus more appropriate to use the results from Fig. 6 only to compare the selectivities of Pd/TiO_2-com-A and Pd/TiO_2-com-R catalysts. The use of anatase TiO_2 as supports for Pd catalysts resulted in positive values of ethylene selectivity while the use of rutile TiO_2 produced ethylene loss due to over-hydrogenation of ethylene to ethane. Ethylene hydrogenation is usually believed to take place on the support by means of a hydrogen transfer mechanism [32]. Thus, the rutile phase of TiO_2 may be responsible for such reaction. Moreover, the presence of Ti^{3+} ions in anatase TiO_2 supports has a positive effect on high ethylene selectivity, i.e. increasing desorption of ethylene from the catalyst surface. It has been reported that the presence of Ti^{3+} on TiO_2 can lower the temperature to induce a strong metal–support interaction [24]. The SMSI between Pd and TiO_2 support can result in lower adsorption strength of ethylene on the catalyst surface and promotes ethylene desorption [21]. There were no such differences in ethylene selectivities for the micron- and the nano-anatase TiO_2 supported Pd catalysts. This indicates that the crystallite size of TiO_2 support did not have a significant impact on ethylene selectivity; the difference in selectivity of ethylene was due mainly to the presence/absence of Ti^{3+} defective sites on the TiO_2 support. However, in the other studies reported previously by our group [25,33], we have found that there was an optimum amount of Ti^{3+} sites to produce high ethylene selectivity since

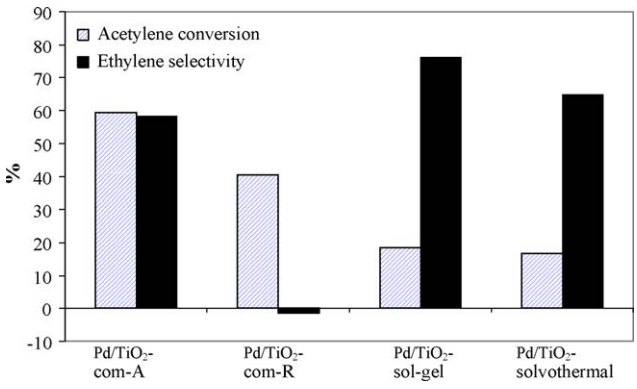

Fig. 6. Catalyst performances in selective acetylene hydrogenation.

only Ti^{3+} species that were in contact with palladium surface promoted SMSI effect and ethylene desorption [24]. Too many Ti^{3+} sites that were not in contact with Pd may result in an over-hydrogenation of ethylene to ethane. This is probably why ethylene selectivity of the Pd/TiO_2-solvothermal is not the highest among four catalysts although the ESR results of Fig. 3 indicated that the intensity of the Ti^{3+} signal was the highest for TiO_2-solvothermal.

4. Conclusions

The use of pure anatase TiO_2 (either micron- or nano-sized) as supports for Pd catalysts produced high ethylene selectivities during selective acetylene hydrogenation in excess ethylene. In contrast, the use of pure rutile TiO_2 supported ones resulted in ethylene loss due to over-hydrogenation of ethylene to ethane. The differences in ethylene selectivity of the various Pd/TiO_2 were due mainly to the presence/absence of the Ti^{3+} defective sites on the TiO_2 support, rather than the difference in the crystallite sizes of the TiO_2 support.

Acknowledgements

Financial supports from the Thailand Research Fund (TRF), Rayong Olefins Co., Ltd., and the Commission on Higher Education are gratefully acknowledged.

References

[1] M.M. Johnson, D.W. Walker, G.P. Nowack, US Patent 4,484,015 (1984).
[2] G.C. Bond, P.B. Wells, J. Catal. 5 (1965) 65.
[3] G.C. Bond, P.B. Wells, Trans. Faraday Soc. 54 (1958) 1537.
[4] M. Larsson, J. Jansson, S. Asplund, J. Catal. 162 (1996) 365.
[5] Y.-J. Huang, C.F. Shun, L.G. Daniel, E.L. Mohundro, J.E. Hartgerink, US Patent 5,332,705 (1994).
[6] K. Flick, C. Herion, H.-M. Allman, US Patent 5,856,262 (1999).
[7] J. Phillips, A. Auroux, G. Bergeret, J. Massardier, A. Renoupez, J. Phys. Chem. 97 (1993) 3565.
[8] D.C. Huang, K.H. Chang, W.F. Pong, P.K. Tseng, K.J. Hung, W.F. Huang, Catal. Lett. 53 (1998) 155.
[9] Q. Zhang, J. Li, X. Liu, Q. Zhu, Appl. Catal. A 197 (2000) 221.
[10] Y. Jin, A.K. Dayte, E. Rightor, R. Gulotty, W. Waterman, M. Smith, M. Holbrook, J. Maj, J. Blackson, J. Catal. 203 (2001) 292.
[11] C. Visser, G.P. Zuidwijk, V. Ponec, J. Catal. 35 (1974) 407.
[12] A. Sarkany, A. Horvath, A. Beck, Appl. Catal. A 229 (2002) 117.
[13] S. LeViness, V. Nair, A. Weiss, J. Mol. Catal. 25 (1984) 131.
[14] E.W. Shin, C.H. Choi, K.S. Chang, Y.H. Na, S.H. Moon, Catal. Today 44 (1998) 137.
[15] Y.H. Park, G.L. Price, Ind. Eng. Chem. Res. 31 (1992) 469.
[16] A. Sarkany, Z. Zsoldos, G. Stefler, W. Hightower, L. Guczi, J. Catal. 157 (1995) 179.
[17] L. Cider, N.-H. Schoon, Ind. Eng. Chem. Res. 30 (1991) 1437.
[18] P. Praserthdam, B. Ngamsom, N. Bogdanchikova, S. Phatanasri, M. Pramotthana, Appl. Catal. A 230 (2002) 41.
[19] B. Ngamsom, N. Bogdanchikova, M.A. Borja, P. Praserthdam, Catal. Commun. 5 (2004) 243.
[20] R.N. Lamb, B. Ngamsom, D.L. Trimm, B. Gong, P.L. Silveston, P. Praserthdam, Appl. Catal. 268 (2004) 43.
[21] J.H. Kang, E.W. Shin, W.J. Kim, J.D. Park, S.H. Moon, J. Catal. 208 (2002) 310.
[22] A. Monzón, E. Romeo, C. Royo, R. Trujillano, F.M. Labajos, V. Rives, Appl. Catal. A 185 (1999) 53.
[23] W.J. Kim, J.H. Kang, I.Y. Ahn, S.H. Moon, J. Catal. 226 (2004) 226.
[24] Y. Li, B. Xu, Y. Fan, N. Feng, A. Qiu, J. Miao, J. He, H. Yang, Y. Chen, J. Mol. Catal. A 216 (2004) 107.
[25] J. Panpranot, L. Nakkararuang, B. Ngamsom, P. Praserthdam, Catal. Lett. 103 (2005) 53.
[26] K. Suriye, P. Praserthdam, B. Jongsomjit, Ind. Eng. Chem. Res. 44 (2005) 6599.
[27] W. Payakgul, O. Mekasuwandumrong, V. Pavarajarn, P. Praserthdam, Ceram. Int. 31 (2005) 391.
[28] F. Zhang, Z. Zheng, D. Liu, Y. Mao, Y. Chen, Z. Zhou, S. Yang, X. Liu, Nucl. Instrum. Meth. B 132 (1997) 620.
[29] J.C. Conesa, P. Malet, G.M. Unuera, J. Sanz, J. Soria, J. Phys. Chem. 88 (1984) 2986.
[30] T.M. Salama, H. Hattori, H. Kita, K. Ebitani, T. Tanaka, J. Chem. Soc. Faraday Trans. 89 (1993) 2067.
[31] Y. Nakaoka, Y. Nosaka, J. Photochem. Photobiol. A 110 (1997) 299.
[32] S. Aplund, J. Catal. 158 (1996) 267.
[33] J. Panpranot, K. Kontapakdee, P. Praserthdam, J. Phys. Chem. B 110 (2006) 8019.
[34] N. Mahata, V. Vishwanathan, J. Catal. 196 (2000) 262.

Available online at www.sciencedirect.com
ScienceDirect
Journal of Crystal Growth 297 (2006) 234–238
JOURNAL OF CRYSTAL GROWTH
www.elsevier.com/locate/jcrysgro

Effect of crystallite size on the surface defect of nano-TiO_2 prepared via solvothermal synthesis

Wilasinee Kongsuebchart, Piyasan Praserthdam*, Joongjai Panpranot, Akawat Sirisuk, Piyawat Supphasrirongjaroen, Chairit Satayaprasert

Center of Excellence on Catalysis and Catalytic Reaction Engineering, Department of Chemical Engineering, Faculty of Engineering, Chulalongkorn University, Bangkok 10330, Thailand

Received 21 June 2006; received in revised form 31 August 2006; accepted 2 September 2006
Communicated by J. M. Redwing
Available online 20 November 2006

Abstract

Nano-TiO_2 powders were synthesized by the solvothermal method under various reaction conditions in order to obtain average crystallite sizes of 9–15 nm. The amounts of surface defect of TiO_2 were measured by means of temperature-programmed desorption of CO_2 and electron spin resonance spectroscopy. It was found that the ratios of surface defect/specific surface area increased significantly with increasing TiO_2 crystallite size. The TiO_2 with higher amounts of surface defects exhibited much higher photocatalytic activity for ethylene decomposition.

Keywords: A1. Crystallite size; A1. Surface defect; A1. Surface structure; B1. TiO_2; B1. Ti^{3+}

1. Introduction

Nowadays, titanium (IV) dioxide or titania (TiO_2) is one of the most popular and promising catalysts in photocatalytic applications for environmental remediation due to the strong oxidizing power of its holes, high photostability, and redox selectivity [1–7]. Titania can be synthesized by various methods such as solvothermal method [8–11], precipitation method [12], sol–gel method [13–15], and thermal decomposition of alkoxide [16]. The properties of TiO_2 synthesized by different methods vary in terms of their crystal structure, chemical composition, surface morphology, crystal defects, specific surface area, etc. While the sol–gel method is widely used to prepare nano-sized TiO_2, the precipitated powders obtained are amorphous in nature and further heat treatment is required for crystallization. The solvothermal method is an alternative route for one-step synthesis of pure anatase nano-sized TiO_2. Particle morphology, crystalline phase, and surface chemistry of the solvothermal-derived TiO_2 can be easily controlled by regulating precursor composition, reaction temperature, pressure, solvent property, and aging time [17].

There always exist structural defects on the surface and inside titania particles [18]. These structural defects are related with the density of photoexcited electrons. Surface defects are good for high photocatalytic activity because they can act as active sites for adsorption and dissociation of molecules on the TiO_2 surface [19–21]. However, the bulk defect lowers the photocatalytic activity because they provide sites for the recombination of the photogenerated electrons. According to electron spin resonance (ESR) spectroscopic study, the photoexcited electron trap at surface Ti^{3+} sites or Ti^{4+} sites within the bulk and holes trap at lattice oxygen ions [22–24]. Therefore, the bulk defect should be reduced to obtain high photocatalytic activity. The nature of defects on TiO_2 can be found in a recent review by Watson et al. [25].

In this study, nano-TiO_2 powders with average crystallite sizes in the range of 9–15 nm were synthesized by the solvothermal method. The effect of crystallite size on the

*Corresponding author. Tel.: +66 2218 6882; fax: +66 2218 6877.
E-mail address: piyasan.p@chula.ac.th (P. Praserthdam).

0022-0248/$ - see front matter © 2006 Elsevier B.V. All rights reserved.
doi:10.1016/j.jcrysgro.2006.09.018

amount of surface defects on TiO_2 was investigated by means of X-ray diffraction (XRD), N_2 physisorption, temperature-programmed desorption of CO_2, and ESR spectroscopy. Photocatalytic activities of the TiO_2 powders were determined from a gas-phase decomposition of ethylene under UV irradiation.

2. Experimental Procedure

2.1. Preparation of TiO_2

Nanocrystalline TiO_2 was prepared using the solvothermal method according to that of Ref. [26] using titanium (IV) *n*-butoxide (TNB) as starting material. In general, 15–25 g of TNB was suspended in 100 cm^3 of toluene in a test tube, which was then placed in a 300 cm^3 autoclave. The gap between the test tube and the autoclave wall was filled with 30 cm^3 of the same solvent used in the test tube. The autoclave was purged completely by nitrogen before heating up to 573 K at a rate of 2.5 K/min. Autogeneous pressure during the reaction gradually increased as the temperature was raised. Once the prescribed temperature was reached, the temperature was held constant for 0.5–8 h. After the system was cooled down, the resulting powders were repeatedly washed with methanol and dried in air. The synthesis product was then calcined in a box furnace by heating up to the desired temperature, in the range of 563–583 K, at a rate of 10 K/min and held at that temperature for 1 h in order to remove any impurity that might remain on the samples after washing with methanol.

2.2. Characterization

Powder XRD analysis was carried out using a SIEMENS D5000 diffractometer with Cu K_α radiation. The crystallite size of the product was determined from broadening of its main peak ($2\theta = 25^\circ$) using the Scherrer equation. The specific surface area was calculated using Brunauer-Emmett-Teller (BET) single-point method on the basis of nitrogen uptake measured at 77 K at a relative pressure of 0.3. Before N_2 adsorption, each sample was dried at 403 K for 30 min in a 30% N_2–helium flow. The amount of nitrogen desorbed was measured using a thermal conductivity detector. Temperature-programmed desorption using CO_2 as a probe molecule (CO_2-TPD) was performed to determine the Ti^{3+} site existing on the surface of a TiO_2 particle [27]. The CO_2-TPD was carried out using homemade equipment composed of a quartz tube in a temperature-controlled bath connecting to a gas chromatograph (GOW-MAC) with a thermal conductivity detector. Approximately 0.05 g of a TiO_2 sample was dosed by 1 vol% CO_2 in helium for 1 h and then desorbed from 143 to 273 K with a rate of 21.5 K/min. ESR spectroscopy was conducted using a JEOL JESRE2X ESR spectrometer. The intensity of ESR was calculated using a computer software program ES-PRIT ESR DATA SYSTEM (version 1.6). Transmission electron micrographs of the TiO_2 samples were obtained using a JEOL JEM 1220 electron microscope operated at 80 kVa.

2.3. Evaluation of photocatalytic activity

The decomposition of ethylene via photocatalytic reaction was employed to evaluate photocatalytic activity of the TiO_2 products obtained. Approximately 0.4 g of the synthesized TiO_2 was spread in a horizontal quartz reactor. The air containing 0.1% ethylene was continuously supplied at a constant flow rate with a gas hourly space velocity of 120 h^{-1}. The reaction temperature was set at 313 K. For each run, an air stream with 0.1% ethylene was first passed through the reactor without illumination until reaching gas–solid adsorption equilibrium (typically 120–180 min) as indicated by identical inlet/outlet ethylene concentration. Then, UV light was illuminated on the surface of the catalyst by using 500 W mercury lamps. The outlet gas was sampled and analyzed at regular intervals by using a SHIMADZU GC-14B gas chromatograph equipped with the flame-ionized detector.

3. Results and discussion

In this study, the crystallite size of the solvothermal-derived TiO_2 was varied in the range of 9–15 nm by changing the concentrations of TNB, the reaction temperatures, and the holding times. Increasing reaction temperature and holding time resulted in an increase in the average crystallite size of TiO_2. The average crystallite sizes and BET surface areas of the obtained TiO_2 from various synthesis conditions are given in Table 1. The XRD patterns of all the obtained TiO_2 powders are shown in Fig. 1. The characteristic peaks of pure anatase-phase titania were observed at 25, 38, and 48° 2θ [28] without contamination of other phases such as rutile and brookite. The average crystallite sizes of TiO_2 were calculated from the full-width at half-maximum of the XRD peak at $2\theta = 25^\circ$ using the Scherrer equation. As the average TiO_2 crystallite size increased from 9 to 15 nm, the BET surface areas decreased monotonically from 126 to 51 m^2/g. The specific surface areas of the TiO_2 samples were also calculated based on the correlation between surface area and crystallite size as follows:

$$S_2 = 6/d\rho,$$

where d is the average crystallite size and ρ is the density of TiO_2 (3.84 g cm^3) [29].

It is noticed that S_1 determined from N_2 physisorption was smaller than S_2 calculated based on the crystallite size for all the TiO_2 samples. This was probably the result of an amorphous-like phase contaminated in the TiO_2 particles [11]. Transmission electron microscope (TEM) imaging has been carried out in order to determine the shape of the particles and the existence of amorphous phase. A typical TEM micrograph of the TiO_2-9 nm sample is shown in Fig. 2. The TEM images show that the TiO_2 products